

Article

Production of a Reinforced Refractory Multielement Alloy via High-Energy Ball Milling and Spark Plasma Sintering

Cinzia Menapace *, Khaja Naib Rasool Shaik, Lorena Emanuelli  and Gloria Ischia 

Department of Industrial Engineering, University of Trento, Via Sommarive 9, 38123 Trento, Italy; khaja.shaik@unitn.it (K.N.R.S.); lorena.emanuelli@unitn.it (L.E.); gloria.ischia@unitn.it (G.I.)

* Correspondence: cinzia.menapace@unitn.it; Tel.: +39-0461-282446; Fax: +39-0461-281977

Abstract: Refractory high entropy alloys have shown potential to be developed as structural materials for elevated temperature applications. In the present research, the multielement alloy Fe₂TiVZrW_{0.5} was produced by high-energy ball milling of elemental powders in the air to promote the formation of reinforcing oxide and nitride particles followed by spark plasma sintering consolidation. The sintering temperature was optimized to achieve a full-density material that was characterized from the microstructural and mechanical points of view. Hardness and KIC were measured in the as-sintered condition as well as after thermal treatment at 1100 °C. TEM observations showed the presence of a fine distribution of ZrO₂ and Ti(V)-N in the microstructure mainly constituted by the bcc Fe-V and Fe-V-W phases. The fine distribution of ceramic particles in a metallic multielement matrix is responsible for the consistent hardness and thermal stability of this alloy.

Keywords: refractory high entropy alloys; ZrO₂; high-energy ball milling; mechanical alloying; spark plasma sintering



Citation: Menapace, C.; Shaik, K.N.R.; Emanuelli, L.; Ischia, G. Production of a Reinforced Refractory Multielement Alloy via High-Energy Ball Milling and Spark Plasma Sintering. *Metals* **2023**, *13*, 1189. <https://doi.org/10.3390/met13071189>

Academic Editor: Elena Gordo

Received: 24 May 2023

Revised: 15 June 2023

Accepted: 22 June 2023

Published: 27 June 2023



Copyright: © 2023 by the authors. Licensee MDPI, Basel, Switzerland. This article is an open access article distributed under the terms and conditions of the Creative Commons Attribution (CC BY) license (<https://creativecommons.org/licenses/by/4.0/>).

1. Introduction

Among the different families of HEAs, refractory ones show very interesting properties. Refractory high-entropy alloys (RHEAs) contain at least four of the nine refractory elements: Cr, Hf, Mo, Nb, Ta, Ti, V, W, and Zr, and have outstanding mechanical strength at extremely high temperatures. They generally have bcc microstructures constituted by elements that have this crystal structure [1,2]. High interest and a great number of studies have recently focused on this class of alloys [1,3–8]. They exhibit remarkable mechanical properties up to 1000 °C and above, and can therefore be considered a valid substitution for Ni-based superalloys as new high-temperature structural materials [9–13]. Refractory HEAs can possess either a single-phase bcc/B2 structure or multi-phase structures in which some intermetallic compounds are dispersed in the bcc/B2 matrix [14–16]. For the production of HEAs, mechanical alloying through a high-energy ball milling process can be used [11,17–21] since the high-energy ball–powder collisions enable the alloying effect among different powders, together with reducing the grain size. Moreover, using the powder metallurgy route, all the problems related to casting (segregations, dendritic microstructure, porosity) can be avoided. To keep the grain size as fine as possible, which ensures high mechanical strength, Spark Plasma Sintering (SPS) can be used to consolidate the powders. SPS is a field-assisted sintering technique similar to conventional hot pressing. However, instead of external heating, a pulsed direct current flows through a graphite die and two graphite punches, which contain the powder, whilst mechanical uniaxial pressure is applied. On increasing temperature under a small pressure (the minimum required to establish the electrical contact between punches and powder), densification is progressively promoted by rearrangement of the powder particles, localized deformation at the contact points, and bulk deformation of the particles [22]. SPS is a suitable method to sinter milled powders since it does not require long times at high temperatures, which

could delete the refining effect obtained through the milling process. Therefore, SPS is a consolidation technique that is used for sintering milled HEA powders since it works with different classes of materials, leading to homogeneous microstructures and high densification in short times [23–26]. The application of the pressure is important to obtain a suitable densification of the compact during the sintering cycle and it was seen that it is more effective if it is applied after powder degassing when the powder particles start to plastically deform [27,28].

One of the main issues concerning materials prepared via ball milling is that they are very sensitive to process conditions (milling type, energy input, type and amount of process control agent, atmosphere, etc.). Specifically, the role of the milling atmosphere is considered of main importance. Several authors have investigated the influence of the milling atmosphere on the formation of secondary phases, on the powder refinement, and on the microstructural evolution of the milled powders [11,17,29–34]. In particular, they have studied the effect of oxygen and nitrogen uptake in the case of milling in air, considering the oxygen adsorption not as a contamination, but as a source of oxides, together with the process control agent and the oxide layers of the initial powders. The intentional oxygen uptake, leading to the formation of oxides, was first developed by Benjamin [35] in the preparation of oxide-dispersion-strengthened superalloys, using a sealed air atmosphere in an attritor mill. Other authors reported that mechanical milling in air promoted the formation of oxides, nitrides, and oxynitrides uniformly dispersed into a metal matrix [11,17,30–34,36]. These compounds are not necessarily harmful to the alloy system since they can contribute to the material dispersion strengthening leading to higher hardness and strength. Moreover, it should be considered that milling in the air is easier and cheaper than using a protective atmosphere; therefore, it is promising for industrial applications.

In the present investigation, powder milling in the air was used to produce a multielement alloy composed of Ti, V, Zr, W, and Fe to take advantage of this milling atmosphere to promote the formation of dispersed reinforcing oxide and nitride particles. Milled powder was spark plasma sintered and characterized in terms of microstructure, hardness, and fracture toughness.

2. Materials and Methods

Five initial high-purity powders (Fisher Scientific, Darmstadt, Germany) were used to produce the alloy Fe₂TiVZrW_{0.5}. The particle size, amount % in weight, and atomic fraction of the initial powders are summarized in Table 1. W powders used have a very small particle size to promote a fine W dispersion into the alloy since in preliminary laboratory experiments it was seen that bigger particles do not allow a complete dissolution of W, even after a prolonged milling time. For the same reason, the alloy composition was not designed in equiatomic proportion (0.2 atomic fraction of each element) but W was reduced to a lower amount, correspondingly increasing the amount of Fe.

Table 1. Initial powders.

| Element | Particle Size (µm) | Purity Level (%) | Weight (wt.%) | Atomic Fraction (-) | VEC (-) |
|---------|--------------------|------------------|---------------|---------------------|---------|
| Fe | <74 | 99.00 | 28.4 | 0.35 | 8 |
| Ti | <149 | 99.90 | 12.2 | 0.18 | 4 |
| V | <44 | 99.50 | 13.0 | 0.18 | 5 |
| Zr | <44 | 99.50 | 23.1 | 0.18 | 4 |
| W | 0.6–0.9 | 99.95 | 23.4 | 0.1 | 6 |

According to the definition proposed by Yeh [37], the ideal configurational entropy of mixing of an alloy ($S^{SS,ideal}$) is calculated with the Formula (1):

$$S^{SS,ideal} = -R \sum c_i \times \ln(c_i) \quad (1)$$

with c_i = atomic fraction of element i .

The $S^{SS,ideal}$ must be higher than 1.5 in order to have a high-entropy alloy. Calculation of S with the atomic fractions reported in Table 1 gives $S = 1.511$.

Another important parameter used to identify high-entropy alloys is the Valence Electron Concentration (VEC). It is used to predict the formation of solid solution phases. The empirical VEC rule was first proposed by Guo et al. [38,39] based on their experimental observation of around 20 multi-component systems such as $Al_xCrCu_yFe_zMnNi$, $Al_xCo_yCr_zCu_{0.5}Fe_wNi_v$, $MoNbTaVW$, and $CoCrFeMnNi$, etc. It was found that FCC is stable at $VEC \geq 8$, BCC is stable at $VEC \leq 6.87$, and a mixture of FCC and BCC phases exists at $6.87 \leq VEC \leq 8$. The calculation of the alloy VEC is based on the VEC values reported in Table 1, and it is carried out through Equation (2) [1]:

$$VEC_{(HEA)} = \sum_{i=1}^n C_i (VEC)_i \quad (2)$$

where C_i and $(VEC)_i$ are the atomic fraction and the VEC of element I , respectively. The present alloy has the following VEC:

$$VEC = \sum C_i \times VEC_i = 5.6 \quad (3)$$

indicating the formation of a bcc solid solution, which is the desired phase for refractory alloys [7,33].

The production of the alloy was carried out through high-energy ball milling and SPS. Ball milling was carried out in a Fritsch Pulverisette six-ball mill (Fritsch, Idar-Oberstein, Germany) with steel vials and balls. A rotation speed of 400 rpm and a ball-to-powder ratio (BPR) of 10 were used. Milling was stopped every 5 h in order to check the powder alloying and refinement. The milling process was carried out in the air to promote oxygen uptake and subsequent oxide formation. To avoid any powder overheating, each milling cycle comprised 20 min of milling followed by a 10 min pause.

Sintering was carried out through Spark Plasma Sintering (DR. SINTER 1050[®] SPS (Sumitomo Coal and Mining Ltd., Tokyo, Japan) at three different temperatures (1050 °C, 1250 °C, and 1350 °C) with a holding time of 5 min at the maximum temperature and applying a pressure of 30 MPa from 650 °C up to the end of the sintering cycle. The heating rate was 50 °C/min. During sintering, the temperature was monitored through a pyrometer recording the temperature from 570 °C.

Thermal treatment was carried out in a tubular laboratory furnace under Ar atmosphere for 1, 4, and 8 h at 900 °C and 1100 °C since the majority of refractory alloys exhibit interesting mechanical properties up to the range 800–1000 °C, showing marked decreases in properties above this temperature [40–42]. Moreover, 1100 °C is considered the highest application temperature of state-of-the-art Ni-based superalloys [43,44], which is a reference alloy category for the RHEAs.

A JEOL IT300 scanning electron microscope (JEOL Ltd., Akishima, Japan) operating at 20 keV accelerating voltage and equipped with an energy-dispersive X-ray spectroscopy (EDXS) was used to examine the powders and the sintered alloys.

X-ray diffraction (XRD) analyses were carried out to evaluate the phase composition after milling and after sintering. The measurements were carried out with an ItalStructures IPD3000 diffractometer (GNR Analytical Instruments Group, Novara, Italy) using $Co K\alpha$ radiation, and an Intel CPS120 detector (Inel, Ardenay, France) that measured the signal concurrently throughout an angular range of 5°–120°. The acquired diffraction spectra

were elaborated by Rietveld's method using MAUD software (Materials Analysis Using Diffraction [45]).

In order to investigate the microstructure, the alloy was also observed with a high-resolution Scanning Transmission Electron Microscope (S/TEM), ThermoFisher Talos F200S (Thermo Fisher Scientific, Waltham, MA, USA) at the maximum accelerating voltage of 200 kV. The instrument is equipped with an EDXS system using two windowless Silicon Drift Detectors (SDD) with a total active area of 60 mm². Thin foils were prepared by starting from 1 mm thick alloy slices, followed by mechanical polishing on both sides down to a thickness of about 70 µm and surface roughness of 1 µm. Three mm discs were punched from the thin foil, and dimple-grinded in the central area down to 20 µm thickness.

The electron transparency was achieved through ion milling in a Leica RES102 apparatus (Leica Microsystems, Wetzlar, Germany) applying an accelerating voltage of 7 kV and a current of 2.6 mA, at a beam incident angle of 5 degrees.

Phase transformations occurring during the heating of the milled powders were studied by means of Differential Scanning Calorimetry (DSC) using a Netzsch STA 409 Luxx apparatus (Netzsch, Selb, Germany) under a protective flux of Argon (100 mL/min) in the chamber. The DSC heating was carried out at 10 °C/min up to 1350 °C, which is the maximum sintering temperature used.

The density of the sintered discs was measured by the water displacement method, and the oxygen content was measured by a LECO TC400 machine (LECO Corporation, St. Joseph, MI, USA). Image Analysis was carried out using the software Image J.

3. Results

3.1. Milled Powders

Powders milled for 5, 10, 15, and 20 h are reported in Figure 1a–d. Powders milled up to 15 h contained large particles formed by cold welding and plastic deformation of different powder particles. The big particles disappeared after 20 h of milling, when particle fragmentation prevails on cold welding [29]. Powder milling of 20 h is shown at a high magnification in Figure 2 with its EDXS. The amount of oxygen and nitrogen adsorbed during the milling process, measured through LECO analysis, are 5.5 %wt. and 6.1 %wt., respectively. As can be seen from Figure 2, powder particles are very fine (<5 µm). X-ray diffraction analysis on the same powder (Figure 3) indicates the presence of two cubic bcc structures, namely 1 and 2 on the XRD spectrum, with a large prevalence of phase bcc 1 (95%) with respect to phase bcc 2 (5%). Phase bcc 1 has a cell size parameter $a = 3.178 \text{ \AA}$ and represents the most part of the alloy, phase bcc 2 has a lower cell size $a = 2.905 \text{ \AA}$ and constitutes only 5% of the alloy. No oxides were detected by XRD thus suggesting that the oxygen detected by LECO is present as a supersaturated solid solution, created by the high-energy milling process, or, as reported by other authors, they are present as amorphous phases [30,46]. There were two sources of oxygen: the initial content of the elemental powders (less than 0.1 %wt. declared by each powder producer) and the atmosphere (air) under which milling was carried out.

3.2. Sintered Samples

3.2.1. Microstructural Analysis

The microstructures of samples sintered at 1250 °C and 1350 °C are shown in Figure 4. The specimen sintered at 1050 °C is not reported because of its excessively high amount of macro-porosity. The sample sintered at 1250 °C also shows the presence of some residual porosity, indicated by arrows in Figure 4a. The amount of porosity measured through Archimedes' method is 3.6 %vol. Instead, the alloy sintered at 1350 °C is almost full density (residual porosity evaluated through Image Analysis < 0.5 %vol.). The microstructure of both specimens, observed under a scanning electron microscope at high magnification (8000×) is very fine and constituted by a homogeneous mix of different light gray, dark gray, and white areas.

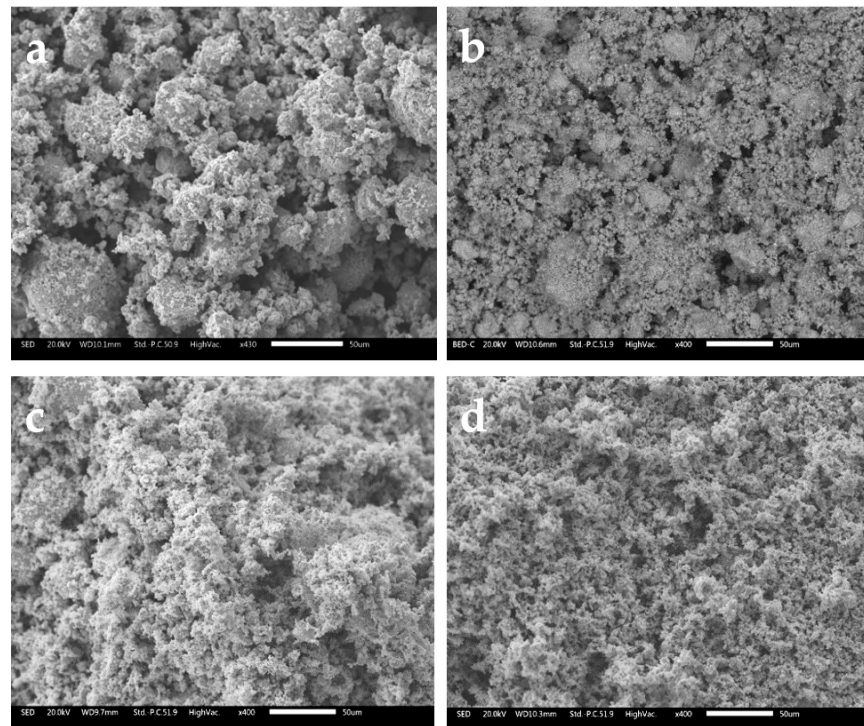


Figure 1. $\text{Fe}_2\text{TiVZrW}_{0.5}$ powder high-energy milled for 5 h (a), 10 h (b), 15 h (c), and 20 h (d).

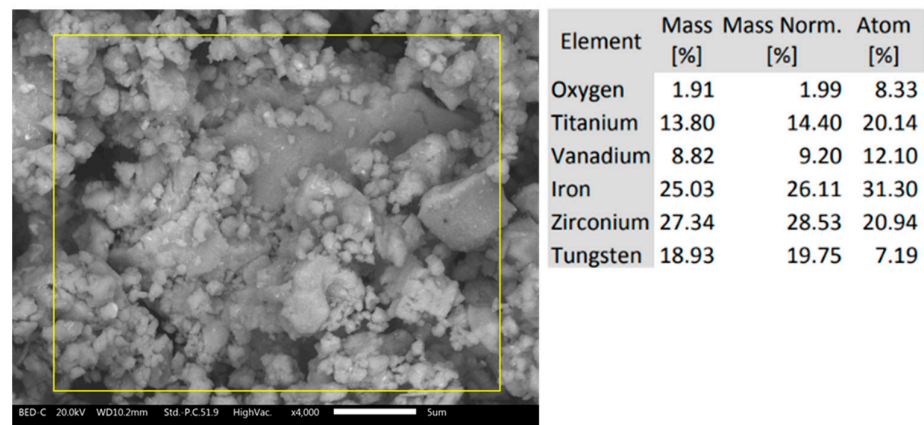


Figure 2. Powders milled for 20 h with EDXS analysis result taken in the area indicated on the micrograph.

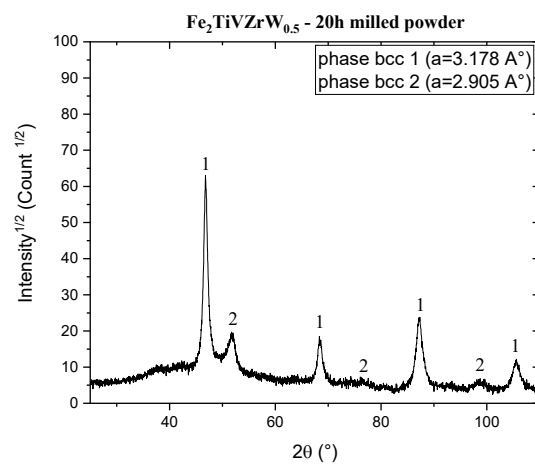


Figure 3. X-Ray diffraction pattern of 20 h milled powder.

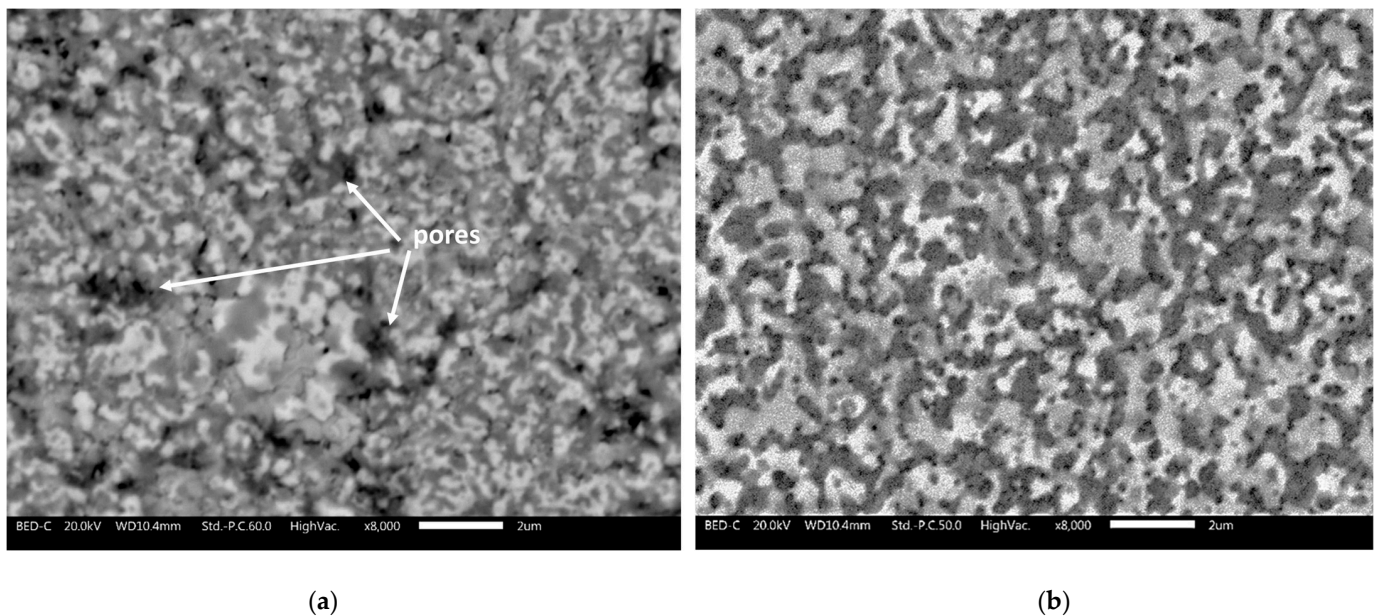


Figure 4. Microstructure of Fe₂TiVZrW_{0.5} sintered at 1250 °C (a) and 1350 °C (b).

LECO analysis on sintered samples revealed an oxygen content of 5.34 %wt. and 5.22 %wt. after sintering at 1250 and 1350 °C, respectively, which are almost the same quantity measured on the milled powder.

Since the material of interest is the one sintered at 1350 °C, because it is full density, on this sample XRD analysis was carried out. The spectrum obtained is shown in Figure 5. As can be seen, there is a complex mix of phases in which only three are clearly detected: Fe-bcc, ZrO₂, and TiN indicated by the numbers 1, 2 and 3 on the XRD spectrum. Other peaks were not identified using the database of known phases.

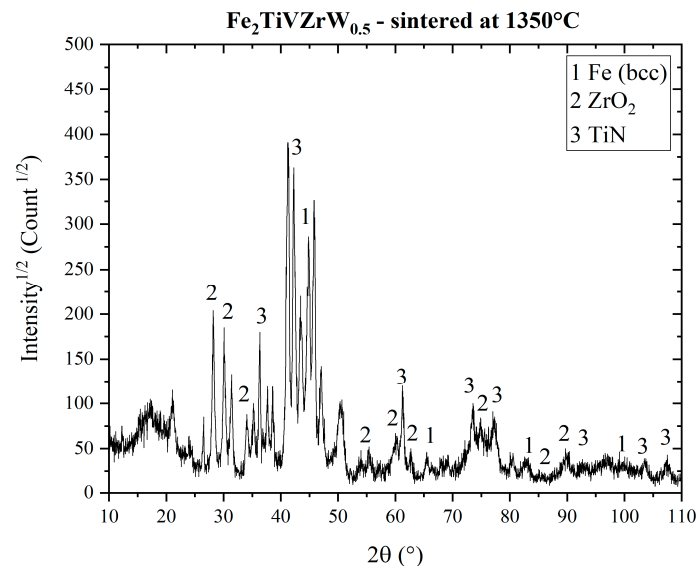


Figure 5. XRD spectrum of Fe₂TiVZrW_{0.5} sintered at 1350 °C.

TEM analysis carried out in different points of the sample sintered at 1350 °C confirmed the very fine grain size of this alloy ranging around 1 µm, as shown in the TEM micrograph of Figure 6. Moreover, through the distribution map of elements (Figure 7) and the corresponding diffraction analysis, four different constituents were identified as documented in Figures 8–12.

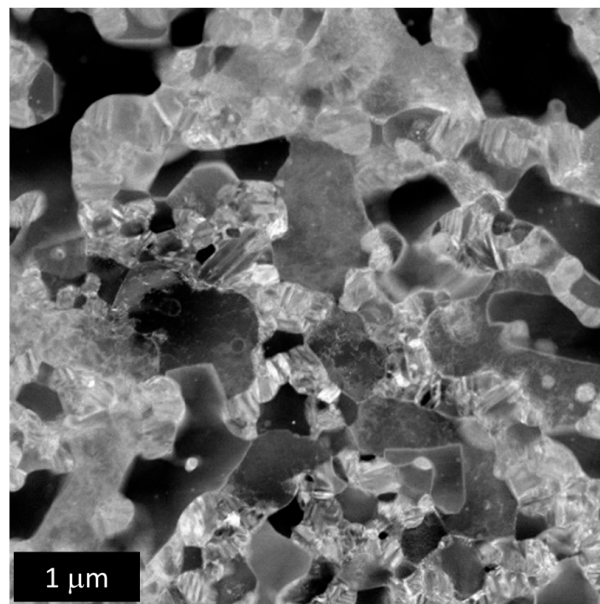


Figure 6. TEM micrograph of sample sintered at 1350 °C.

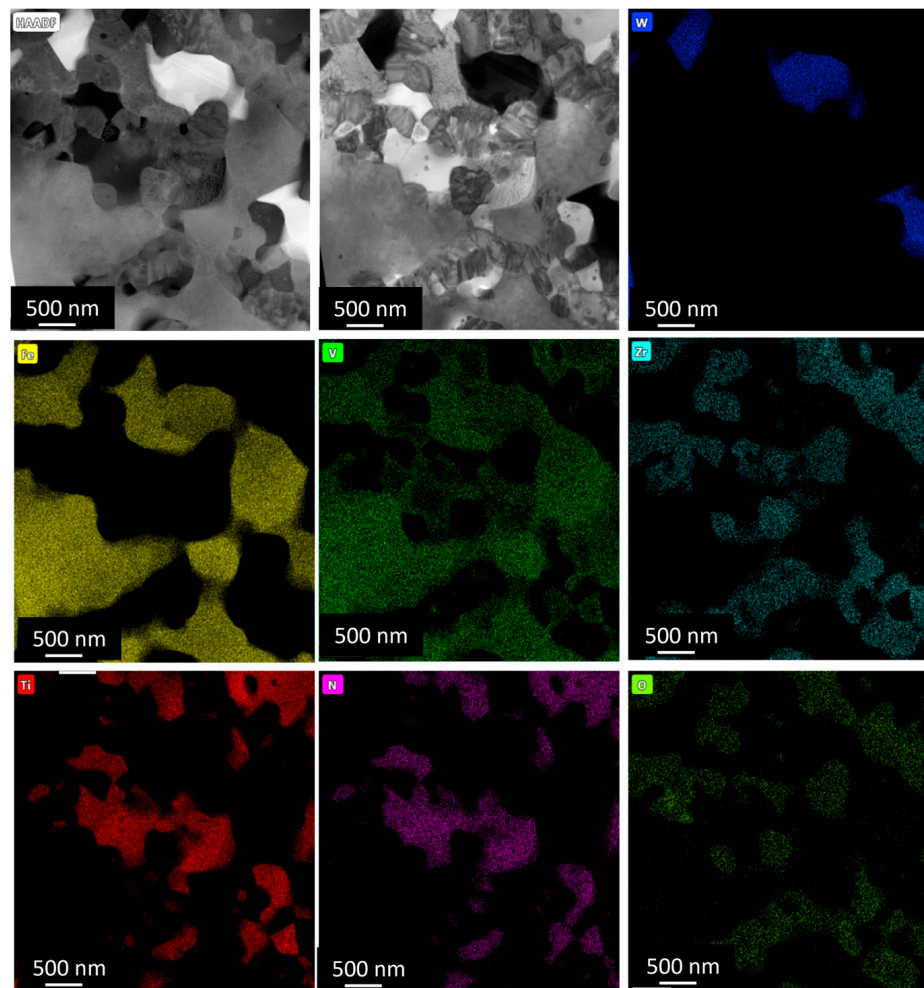


Figure 7. Distribution map of elements.

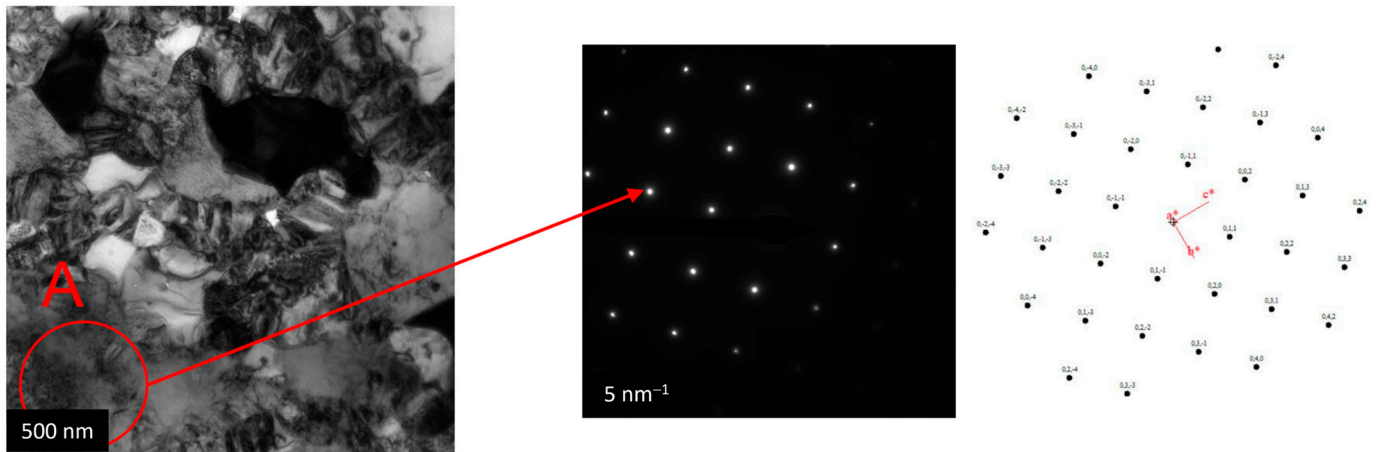


Figure 8. Identification of area A containing Fe and V and having a bcc structure (Fe bcc ZA 1 0 0).

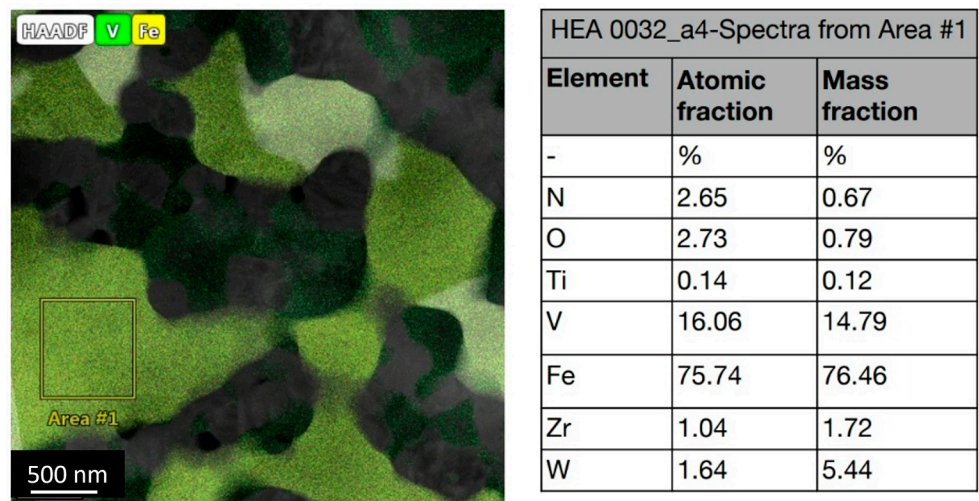


Figure 9. EDXS analysis carried out on an F-V bcc area.

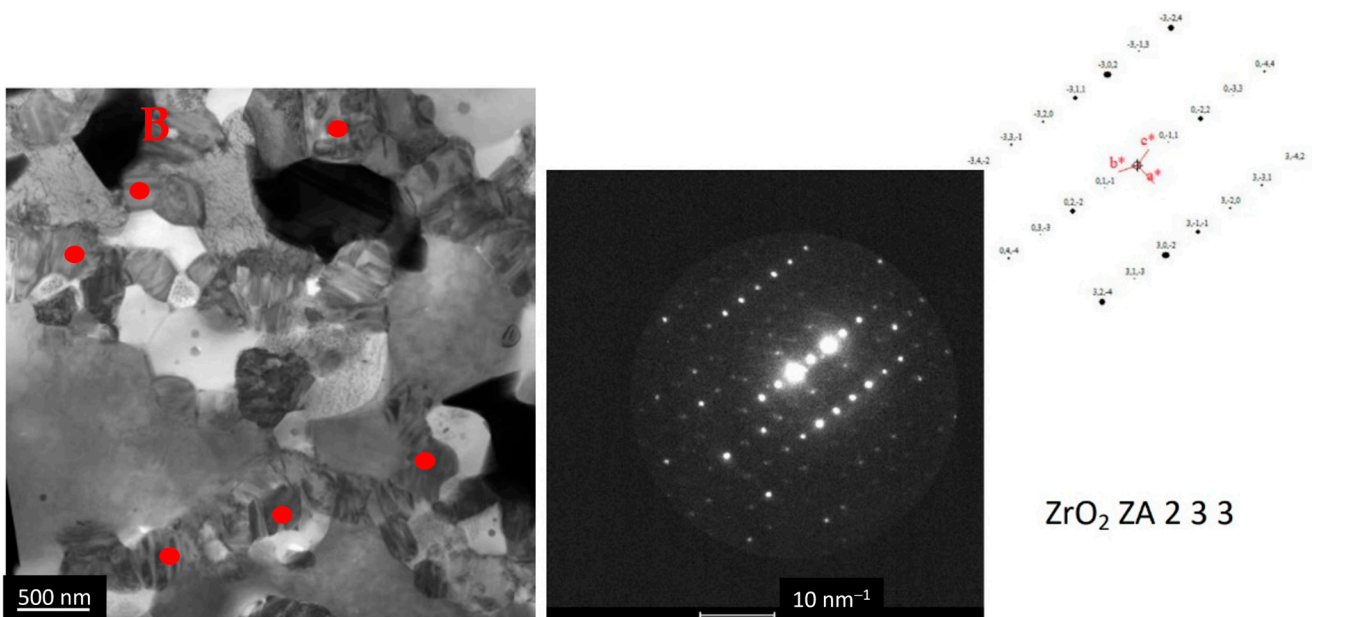


Figure 10. Identification of B particles, indicated by red dots, as monoclinic ZrO_2 . * is a B, referring to the phase B.

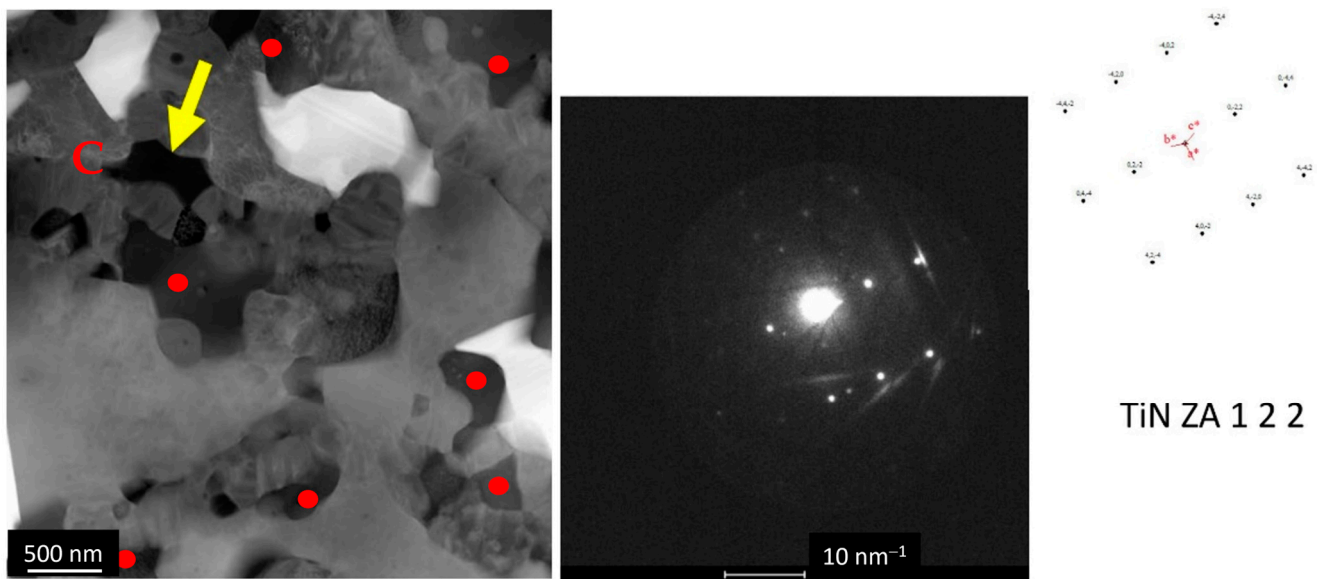


Figure 11. Identification of C particles, indicated by red dots, as cubic Ti(V)-N.

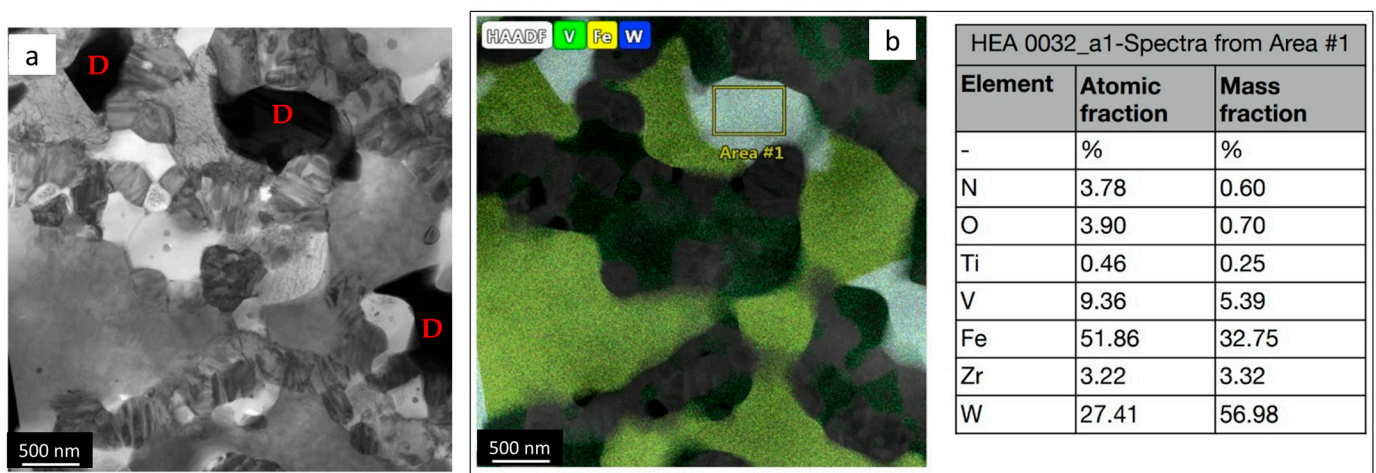


Figure 12. (a) D areas containing Fe-W-V (b) EDXS analysis on one of these areas.

The four phases identified and indicated with the letters A-B-C-D in Figures 8–12 are as follows:

- A. Fe-V bcc phase (Figures 8 and 9);
- B. ZrO₂ monoclinic (Figure 10);
- C. Ti(V)-N cubic (Figure 11);
- D. Fe-V-W phase (Figure 12).

Fe-V bcc, ZrO₂, and Ti(V)-N phases are ascribed to the three phases also detected by XRD analysis. Differently, Fe-V-W results were undetected on the XRD spectrum due to the limitation of the MAUD database. The presence of ZrO₂ and Ti(V)-N particles in the Fe-V phase creates a sort of composite material in which hard particles are homogeneously distributed into a soft “matrix” as can be observed in Figures 9 and 10. The Fe-V system containing an amount of V up to about 20 %wt. is a soft bcc solid solution having a hardness of 200 HV, while for higher V contents a thermal treatment above 700 °C induces the formation of σ phase with a consequent hardening [47]. In the present investigation, the F-V phase contained about 15 %wt. of V, as indicated by EDXS analysis carried out on different F-V areas. One of them is reported in Figure 9.

As can be seen in Figure 10, which shows some ZrO₂ particles, there was an evident twinning in these oxides. Monoclinic ZrO₂ was mostly twinned on (1 1 0) and (1 0 0)

planes [48]. The ZrO_2 particles measured on TEM images had a mean size of about 300 nm, they were homogeneously distributed in the matrix, and their total amount, measured through Image Analysis on EDXS maps, was 18% vol. These features, together with the fine grain size of the other phases, are responsible for the high hardness of this alloy and the hardness stability at high temperatures. Zirconia is stable up to very high temperatures, about 1250 °C in working conditions [49]. Regarding the Fe-V-W phase, EDXS analysis indicates the presence of about 57 %wt. W, 33 %wt. Fe and 5 %wt. V, as shown in Figure 12b.

Moreover, in addition to the four phases (A–D), a fifth phase was identified, corresponding to spongy areas homogeneously distributed in the material, as shown in Figure 13. These areas contain the five elements constituting the alloy. Due to the complexity of the system, it was not possible to index the diffraction pattern with the structure present in the database containing these elements.

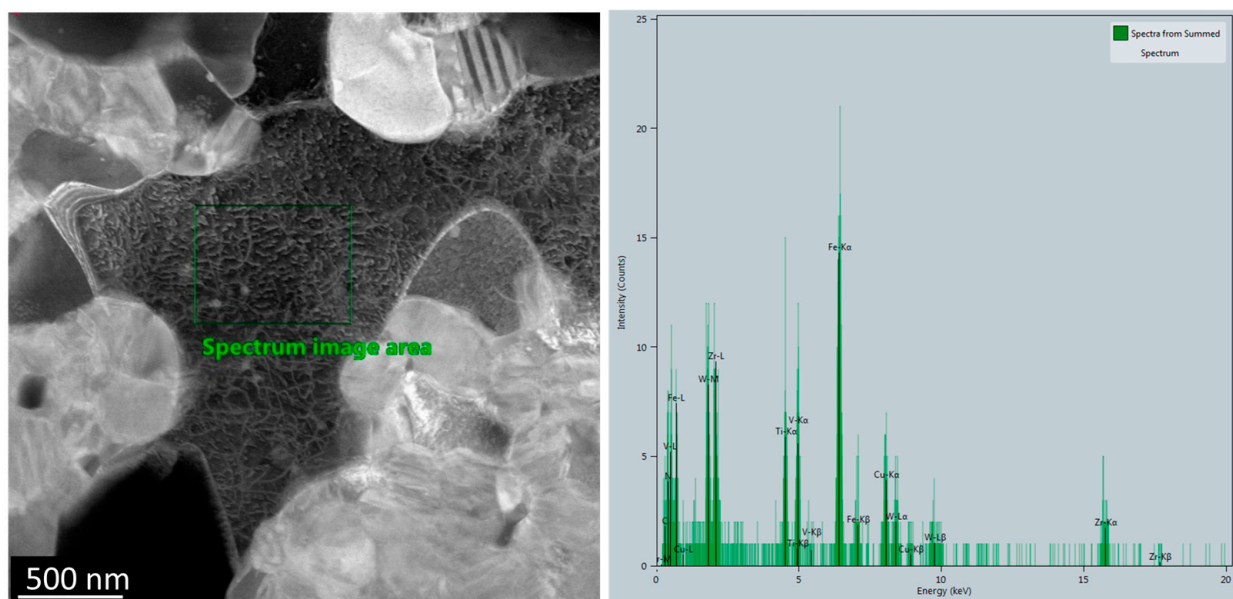


Figure 13. EDXS analysis of a spongy area containing all the alloy constituent elements.

3.2.2. Hardness and Fracture Toughness

The hardness of the samples sintered at 1250 °C and 1350 °C are 1316 and 1348 HV5, respectively. Hardness maintained remarkable values even after 8 h at 1100 °C (852 HV5). Similar behavior was also observed by Sathiyamoorthi et al. [50] who found a very stable hardness in temperature in a high entropy alloy with different composition but similar microstructural features, i.e., constituted by a very fine fcc matrix reinforced by the precipitation of carbides and oxides.

Hardness values were used to calculate KIC through Equation (3) proposed by Shubert et al. which refers to the Palmqvist method [51]:

$$K_{IC} = 0.0028 \cdot \sqrt{H} \cdot \sqrt{\frac{P}{\sum l_i}} \quad (3)$$

where H = Vickers hardness in N/mm^2 , P = load in N , l_i = crack lengths in mm .

An example of hardness indentation with cracks starting at the corners of the imprint, used for the calculation of KIC, is shown in Figure 14. The KIC values found were 3.55 and 3.97 $MPa \cdot m^{1/2}$ for the samples sintered at 1250 and 1350 °C, respectively. The very low values of fracture toughness are more similar to those of ceramic materials than metals due to the presence of ZrO_2 and TiN and the intrinsic brittleness of the two phases that can be considered at high entropy (Fe-W-V and the spongy Fe-W-V-Ti-Zr). While, for example, Al_2O_3 in Al alloys contributes to significant improvements in strength, fracture toughness,

stress corrosion resistance, and fatigue crack growth [29,52], in the present investigation ZrO_2 formed in a matrix constituted by highly disordered phases (Fe-V-W and Fe-V-W-Ti-Zr), which were not ductile. For this reason, its contribution to the improvement of fracture toughness is counterbalanced by a growing brittleness.

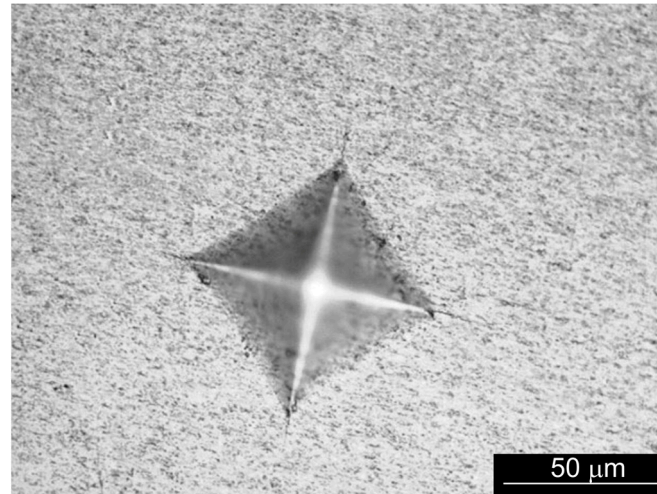


Figure 14. Micrographs of a Vickers indentation and induced cracks at the corners.

Hardness and KIC values of the samples sintered at 1350 °C and heat-treated at 900 °C and 1100 °C for different times are reported in Figure 15 and Table 2, respectively.

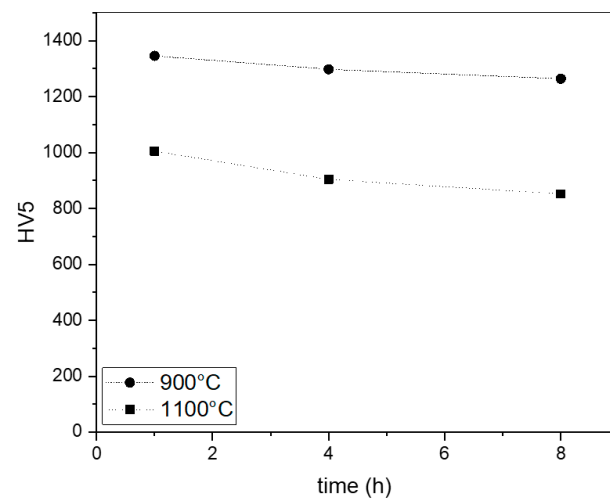


Figure 15. Hardness values after heat treatments at 900 °C and 1100 °C.

Table 2. KIC values of samples heat treated at 900 °C and 1100 °C.

| treatment time | KIC Measured through Palmqvist Method MPa m ^{1/2} | |
|----------------|---|-------------|
| | T = 900 °C | T = 1100 °C |
| 1 h | 4.10 | 5.05 |
| 4 h | 4.68 | 5.71 |
| 8 h | 4.87 | 5.90 |

Hardness values showed a consistent decrease only at 1100 °C, remaining anyway above 850 HV5. KIC after 8 h at 1100 °C increased to 5.90 MPa m^{1/2}, but it was still a quite low value. KIC data presented in the review by Li [52] varied between less than 1 to more

than 200 MPa m^{1/2} depending on the alloy composition, phase constituents, processing methods, and temperature. KIC represents a key issue to be improved for the application of these alloys in different fields, particularly in structural engineering parts.

3.3. Sintering Behavior

The sintering behavior of the milled powder was studied by analyzing different parameters recorded during the whole SPS process: voltage applied, current flowing through the sample, displacement of the SPS lower punch, and its displacement rate.

The current flowing vs. voltage applied is shown in Figure 16. This curve was smooth and continuous, indicating the absence of any oxide layer breakdown. The breakdown of the oxide layer covering the powder particles was revealed by a sudden change in slope and an evident curve discontinuity and irregularity [53]. This confirms the absence of a surface oxide layer on the milled powder particles (in line with XRD data of Figure 3) and the presence of oxygen as a supersaturated solid solution that forms oxides particles on heating (i.e., during the sintering cycle) as confirmed by XRD data of Figure 5 and by the TEM investigation.

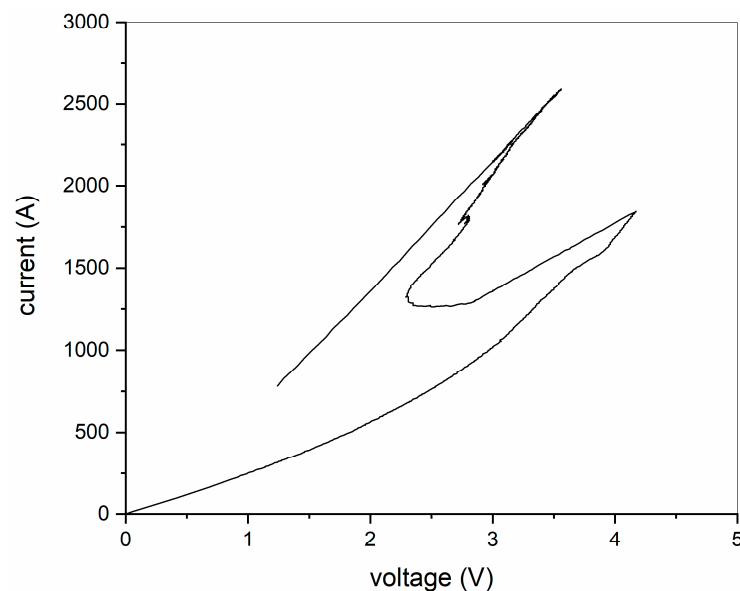


Figure 16. Current vs. voltage during the sintering cycle.

In Figure 17 the displacement of the SPS lower punch is shown as a function of the temperature. The displacement rate is also reported. It is interesting to observe that the displacement increased up to 1280 °C where the slope started to decrease since the densification process was slowing down and going to finish. At the sintering temperature of 1250 °C the densification was not completed; therefore, residual porosity was present in the alloy sintered at this temperature, as indicated in Figure 4a. At 1350 °C the sintered sample was instead almost full density. Regarding the displacement rate reported in Figure 17, it can be observed that it showed three peaks. These points correspond to maximum densification rate points, i.e., temperatures at which the particles' accommodation, plastic deformation, phase transformations, and local sintering of the powders promote densification processes. The highest peak of the displacement rate (i.e., densification rate) was observed at 1222 °C. This peak indicates the occurrence of high-temperature plastic deformation, which is the main mechanism of consolidation and densification of this material. The temperature required to deform the powder compact is quite high because of the hardness of the milled powder related to its fine grain size, the alloying effect, and the dispersion of fine oxides formed during the heating step of the sintering process (up to this temperature).

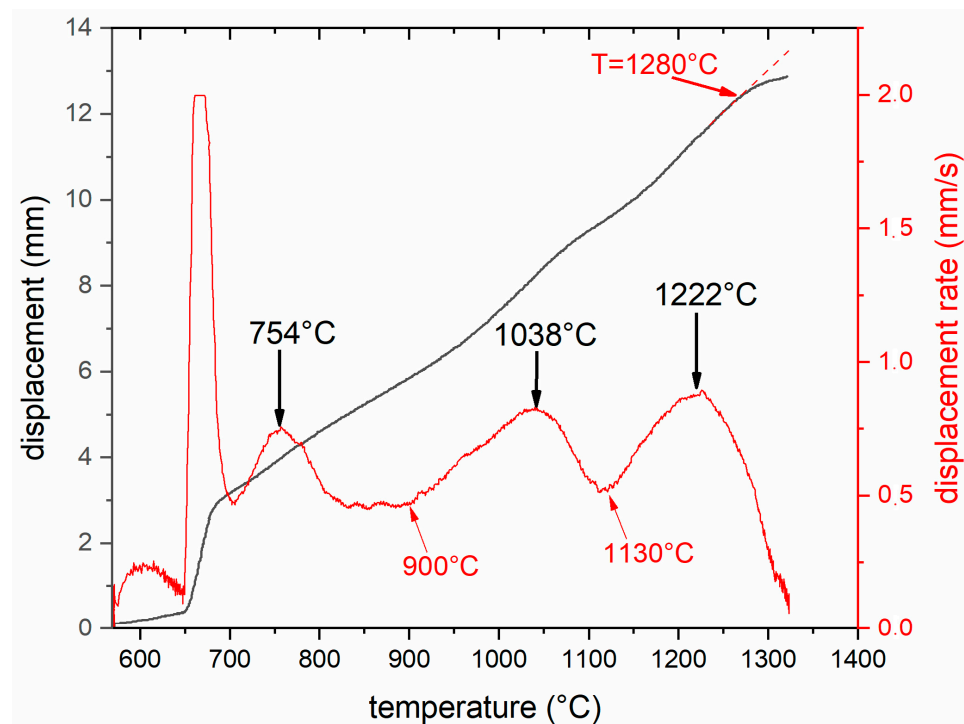


Figure 17. Displacement and displacement rate vs. temperature during the sintering cycle.

DSC analysis carried out on the milled powder is reported in Figure 18. It shows four peaks, indicated by the numbers 1–4 on the curve. The first peak was exothermic and centered at 400 °C, the second was also exothermic and started at 740 °C. Peak 3 was the only endothermic peak as shown in the square graph at higher magnification, and it started at about 1120 °C and had its minimum at 1170 °C. The last peak (4) was exothermic and showed its maximum at 1274 °C.

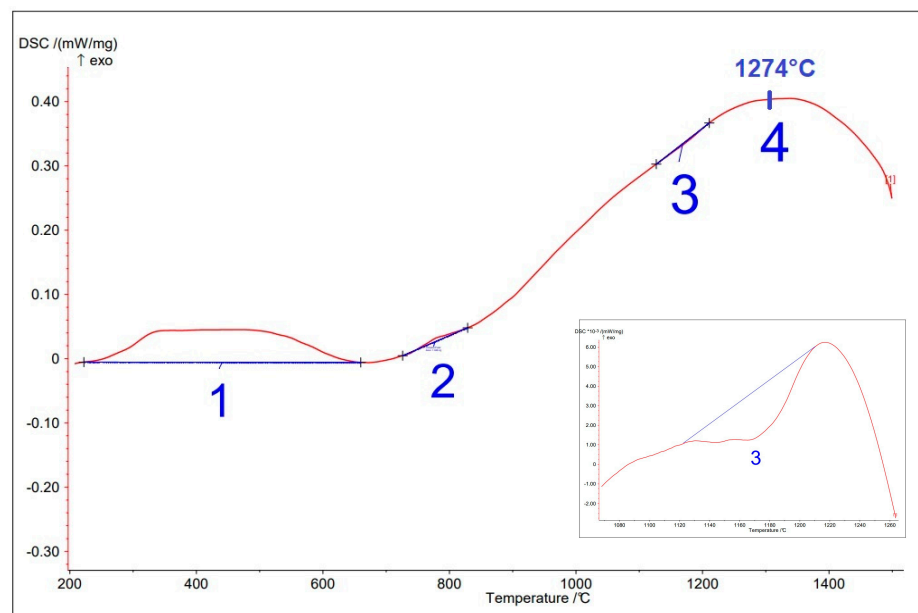


Figure 18. DSC curve of the milled powder.

Peak 1 is ascribed to the formation of TiN [32,54–56]. Peak 2 can be due to the precipitation of ZrO₂ from the oxygen-rich supersaturated solid solution [57], which increases the hardness of the alloy slowing down the phenomena of plastic deformation of the powder

particles responsible for sintering, indicated by a reduction of the displacement rate, as shown in Figure 17. A decrease in the displacement rate was observed starting from 754 °C. The endothermic peak 3 was due to the transformation of the crystal structure of ZrO₂ from monoclinic to tetragonal [58] which led to a corresponding increase of ductility and reduction in volume that resulted in the displacement rate increase observed in Figure 17, which had a maximum at 1222 °C [59]. Above this temperature, the densification rate started to decrease but sintering was still ongoing (the sample sintered at 1250 °C still had some residual porosity). Lastly, the exothermic peak 4 is attributed to the sintering process of the powders at the end of the DSC test which, even without any pressure applied, were no more dispersed but consolidated into the crucible. The heat released on sintering was very small and showed its maximum at a temperature (1274 °C) which is in line with the temperature of the deviation of displacement from the linearity observed in Figure 17 (1280 °C), which indicates the consolidation and densification of the powder compact.

4. Conclusions

A multielement refractory alloy was produced through high-energy ball milling of elemental powders in an air atmosphere, followed by spark plasma sintering consolidation. After 20 h of milling, an almost homogeneous bcc structure was obtained that evolved into a multiphase system during the sintering cycle, in which reinforcing particles such as ZrO₂ and TiN formed due to the oxygen and nitrogen uptake that occurred during the milling process. The sintering temperature was optimized to obtain a full-density material. The very fine multiphase microstructure of this alloy, analyzed through a TEM microscope, comprised particles of ZrO₂ and TiN dispersed in a matrix made of three different phases and showed a very high hardness stable with temperature.

Author Contributions: Conceptualization, C.M., L.E. and K.N.R.S.; methodology, C.M. and G.I.; formal analysis, K.N.R.S. and L.E.; investigation, C.M. and K.N.R.S.; resources, C.M.; writing—original draft preparation, C.M., K.N.R.S. and L.E.; writing—review and editing, C.M., L.E. and G.I.; supervision, C.M. All authors have read and agreed to the published version of the manuscript.

Funding: This research received no external funding.

Data Availability Statement: The data presented in this study are available on request from the corresponding author.

Conflicts of Interest: The authors declare no conflict of interest.

References

1. Gao, M.C.; Liaw, P.K.; Yeh, J.W.; Zhang, Y. *High-Entropy Alloys: Fundamentals and Applications*; Springer: Berlin, Germany, 2016.
2. Liu, F.; Liaw, P.K. Recent Progress with BCC-Structured High-Entropy Alloys. *Metals* **2022**, *12*, 501. [[CrossRef](#)]
3. Gao, X.; Wang, L.; Guo, N.; Luo, L.; Zhu, G.; Shi, C.; Su, Y.; Guo, J. Microstructure and Mechanical Properties of Multi-Phase Reinforced Hf-Mo-Nb-Ti-Zr Refractory High-Entropy Alloys. *Int. J. Refract. Met. Hard Mater.* **2022**, *102*, 105723. [[CrossRef](#)]
4. Real, C.; Alcalá, M.D.; Trigo, I.; Fombella, I.; Córdoba, J.M. Fabrication and Characterization of FeCoNiCrMn,(Al) High Entropy Alloy Based (Ti,Ta,Nb)(C,N) Cermet. *Int. J. Refract. Met. Hard Mater.* **2021**, *101*, 105694. [[CrossRef](#)]
5. Liu, Z.; Shi, X.; Zhang, M.; Qiao, J. Development of Refractory High Entropy Alloys with Tensile Ductility at Room Temperature. *Metals* **2023**, *13*, 329. [[CrossRef](#)]
6. Senkov, O.; Miracle, D.; Chaput, K.; Couzinie, J. Development and exploration of refractory high entropy alloys—A review. *J. Mat. Res.* **2018**, *33*, 3092–3128. [[CrossRef](#)]
7. Pickering, E.J.; Carruthers, A.W.; Barron, P.J.; Middleburgh, S.C.; Armstrong, D.E.J.; Gandy, A.S. High-Entropy Alloys for Advanced Nuclear Applications. *Entropy* **2021**, *23*, 98. [[CrossRef](#)]
8. Tian, Y.-S.; Zhou, W.-Z.; Tan, Q.-B.; Wu, M.-X.; Qiao, S.; Zhu, G.-L.; Dong, A.-P.; Shu, D.; Sun, B.-D. A Review of Refractory High-Entropy Alloys. *Trans. Nonferrous Met. Soc. China* **2022**, *32*, 3487–3515. [[CrossRef](#)]
9. Chen, S.; Qi, C.; Liu, J.; Zhang, J.; Wu, Y. Recent Advances in W-Containing Refractory High-Entropy Alloys—An Overview. *Entropy* **2022**, *24*, 1553. [[CrossRef](#)]
10. Senkov, O.N.; Wilks, G.B.; Miracle, D.B.; Chuang, C.P.; Liaw, P.K. Refractory High-Entropy Alloys. *Intermetallics* **2010**, *18*, 1758–1765. [[CrossRef](#)]
11. Li, Q.; Zhang, H.; Li, D.; Chen, Z.; Qi, Z. The Effect of Configurational Entropy on Mechanical Properties of Single BCC Structural Refractory High-Entropy Alloys Systems. *Int. J. Refract. Met. Hard Mater.* **2020**, *93*, 105370. [[CrossRef](#)]

12. Vlasák, T.; Čížek, J.; Melikhova, O.; Lukáč, F.; Preisler, D.; Janeček, M.; Harcuba, P.; Zimina, M.; Srba, O. Thermal Stability of Microstructure of High-Entropy Alloys Based on Refractory Metals Hf, Nb, Ta, Ti, V, and Zr. *Metals* **2022**, *12*, 394. [[CrossRef](#)]
13. Lu, S.; Li, X.; Liang, X.; Yang, W.; Chen, J. Effect of V and Ti on the Oxidation Resistance of WmotaNb Refractory High-Entropy Alloy at High Temperatures. *Metals* **2022**, *12*, 41. [[CrossRef](#)]
14. Yurchenko, N.Y.; Stepanov, N.D.; Gridneva, A.O.; Mishunin, M.V.; Salishchev, G.A.; Zhrebtsov, S.V. Effect of Cr and Zr on Phase Stability of Refractory Al-Cr-Nb-Ti-V-Zr High-Entropy Alloys. *J. Alloys Compd.* **2018**, *757*, 403–414. [[CrossRef](#)]
15. Senkov, O.N.; Miracle, D.B.; Chaput, K.J.; Couzinie, J.P.; Yurchenko, N.Y.; Stepanov, N.D.; Gridneva, A.O.; Mishunin, M.V.; Salishchev, G.A.; Zhrebtsov, S.V.; et al. Phase Stability in High Entropy Alloys: Formation of Solid-Solution Phase or Amorphous Phase. *Powder Metall.* **2018**, *61*, 115–122.
16. Chen, H.; Kauffmann, A.; Seils, S.; Boll, T.; Liebscher, C.H.; Harding, I.; Kumar, K.S.; Szabó, D.V.; Schlabach, S.; Kauffmann-Weiss, S.; et al. Crystallographic Ordering in a Series of Al-Containing Refractory High Entropy Alloys Ta-Nb-Mo-Cr-Ti-Al. *Acta Mater.* **2019**, *176*, 123–133. [[CrossRef](#)]
17. Moravcik, I.; Kubicek, A.; Moravcikova-Gouvea, L.; Adam, O.; Kana, V.; Pouchly, V.; Zadera, A.; Dlouhy, I. The Origins of High-Entropy Alloy Contamination Induced by Mechanical Alloying and Sintering. *Metals* **2020**, *10*, 1186. [[CrossRef](#)]
18. Xiong, W.; Guo, A.X.Y.; Zhan, S.; Liu, C.T.; Cao, S.C. Refractory High-Entropy Alloys: A Focused Review of Preparation Methods and Properties. *J. Mater. Sci. Technol.* **2023**, *142*, 196–215. [[CrossRef](#)]
19. Yang, Q.; Tang, Y.; Wen, Y.; Zhang, Q.; Deng, D.; Nai, X. Microstructures and Properties of CoCrCuFeNiMox High-Entropy Alloys Fabricated by Mechanical Alloying and Spark Plasma Sintering. *Powder Metall.* **2018**, *61*, 115–122. [[CrossRef](#)]
20. Zhang, M.; Zhang, W.; Liu, Y.; Liu, B.; Wang, J. FeCoCrNiMo High-Entropy Alloys Prepared by Powder Metallurgy Processing for Diamond Tool Applications. *Powder Metall.* **2018**, *61*, 123–130. [[CrossRef](#)]
21. Shkodich, N.; Sedegov, A.; Kuskov, K.; Busurin, S.; Scheck, Y.; Vadchenko, S.; Moskovskikh, D. Refractory High-Entropy HfTaTiNbZr-Based Alloys by Combined Use of Ball Milling and Spark Plasma Sintering: Effect of Milling Intensity. *Metals* **2020**, *10*, 1268. [[CrossRef](#)]
22. Diouf, S.; Menapace, C.; Molinari, A. Study of Effect of Particle Size on Densification of Copper during Spark Plasma Sintering. *Powder Metall.* **2012**, *55*, 228–234. [[CrossRef](#)]
23. Fu, Z.; Chen, W.; Xiao, H.; Zhou, L.; Zhu, D.; Yang, S. Fabrication and Properties of Nanocrystalline Co_{0.5}FeNiCrTi_{0.5} High Entropy Alloy by MA-SPS Technique. *Mater. Des.* **2013**, *44*, 535–539. [[CrossRef](#)]
24. Wang, C.; Ji, W.; Fu, Z. Mechanical Alloying and Spark Plasma Sintering of CoCrFeNiMnAl High-Entropy Alloy. *Adv. Powder Technol.* **2014**, *25*, 1334–1338. [[CrossRef](#)]
25. Fang, S.; Chen, W.; Fu, Z. Microstructure and Mechanical Properties of Twinned Al_{0.5}CrFeNiCo_{0.3}Co_{0.2} High Entropy Alloy Processed by Mechanical Alloying and Spark Plasma Sintering. *Mater. Des.* **2014**, *54*, 973–979. [[CrossRef](#)]
26. Joo, S.H.; Kato, H.; Jang, M.J.; Moon, J.; Kim, E.B.; Hong, S.J.; Kim, H.S. Structure and Properties of Ultrafine-Grained CoCrFeMnNi High-Entropy Alloys Produced by Mechanical Alloying and Spark Plasma Sintering. *J. Alloys Compd.* **2017**, *698*, 591–604. [[CrossRef](#)]
27. Diouf, S.; Menapace, C.; D’Incau, M.; Molinari, A.; Ischia, G. Spark Plasma Sintering of Cryomilled Copper Powder. *Powder Metall.* **2013**, *56*, 420–426. [[CrossRef](#)]
28. Straffelini, G.; Nogueira, A.P.; Muterlle, P.; Menapace, C. Spark Plasma Sintering and Hot Compression Behaviour of AZ91 Mg Alloy. *Mater. Sci. Technol.* **2011**, *27*, 1582–1587. [[CrossRef](#)]
29. Suryanarayana, C. Mechanical Alloying and Milling. *Prog. Mater. Sci.* **2001**, *46*, 1–184. [[CrossRef](#)]
30. Cuevas, F.G.; Cintas, J.; Montes, J.M.; Gallardo, J.M. Powder Metallurgy On Selection of Milling Atmosphere for Production of Al-10%Ti Powders On Selection of Milling Atmosphere for Production of Al-10%Ti Powders. *Powder Metall.* **2009**, *52*, 116–123. [[CrossRef](#)]
31. Rajendrachari, S. An Overview of High-Entropy Alloys Prepared by Mechanical Alloying Followed by the Characterization of Their Microstructure and Various Properties. *Alloys* **2022**, *1*, 116–132. [[CrossRef](#)]
32. Lu, C.J.; Zhang, J.; Li, Z.Q. Structural Evolution of Titanium Powder during Ball Milling in Different Atmospheres. *J. Alloys Compd.* **2004**, *381*, 278–283. [[CrossRef](#)]
33. Olier, P.; Couvrat, M.; Cayron, C.; Lochet, N.; Chaffron, L. Incidence of Mechanical Alloying Contamination on Oxides and Carbides Formation in ODS Ferritic Steels. *J. Nucl. Mater.* **2013**, *442*, S106–S111. [[CrossRef](#)]
34. Noh, S.; Choi, B.K.; Kang, S.H.; Kim, T.K. Influence of Mechanical Alloying Atmospheres on the Microstructures and Mechanical Properties of 15Cr Ods Steels. *Nucl. Eng. Technol.* **2014**, *46*, 857–862. [[CrossRef](#)]
35. Benjamin, J.S. Dispersion Strengthened Superalloys by Mechanical Alloying. *Metall. Trans.* **1970**, *1*, 2943–2951. [[CrossRef](#)]
36. Liu, W.H.; Lu, Z.P.; He, J.Y.; Luan, J.H.; Wang, Z.J.; Liu, B.; Liu, Y.; Chen, M.W.; Liu, C.T. Ductile CoCrFeNiMox High Entropy Alloys Strengthened by Hard Intermetallic Phases. *Acta Mater.* **2016**, *116*, 332–342. [[CrossRef](#)]
37. Yeh, J.W. Recent Progress in High-Entropy Alloys. *Ann. Chim. Sci. Mater.* **2006**, *31*, 633–648. [[CrossRef](#)]
38. Guo, S.; Liu, C.T. Phase Stability in High Entropy Alloys: Formation of Solid-Solution Phase or Amorphous Phase. *Prog. Nat. Sci. Mater. Int.* **2011**, *21*, 433–446. [[CrossRef](#)]
39. Guo, S.; Ng, C.; Lu, J.; Liu, C.T. Effect of Valence Electron Concentration on Stability of Fcc or Bcc Phase in High Entropy Alloys Related Articles Effect of Valence Electron Concentration on Stability of Fcc or Bcc Phase in High Entropy Alloys. *Addit. Inf. J. Appl. Phys. J. Homepage* **2011**, *109*, 144503.

40. Senkov, O.N.; Gorsse, S.; Miracle, D.B. High Temperature Strength of Refractory Complex Concentrated Alloys. *Acta Mater.* **2019**, *175*, 394–405. [CrossRef]
41. Senkov, O.N.; Jensen, J.K.; Pilchak, A.L.; Miracle, D.B.; Fraser, H.L. Compositional Variation Effects on the Microstructure and Properties of a Refractory High-Entropy Superalloy AlMo_{0.5}NbTa_{0.5}TiZr. *Mater. Des.* **2018**, *139*, 498–511. [CrossRef]
42. Srikanth, M.; Raja Annamalai, A.; Muthuchamy, A.; Jen, C.P. A Review of the Latest Developments in the Field of Refractory High-Entropy Alloys. *Crystals* **2021**, *11*, 612. [CrossRef]
43. Atli, K.C.; Karaman, I. A Short Review on the Ultra-High Temperature Mechanical Properties of Refractory High Entropy Alloys. *Front. Met. Alloy.* **2023**, *2*, 1135826. [CrossRef]
44. Rame, J.; Utada, S.; Bortoluci Ormastroni, L.M.; Mataveli-Suave, L.; Menou, E.; Després, L.; Kontis, P.; Cormier, J. Platinum-Containing New Generation Nickel-Based Superalloy for Single Crystalline Applications. In Proceedings of the Minerals, Metals and Materials Series, Seven Springs, PA, USA, 13–17 September 2020.
45. Rietveld, H.M. A Profile Refinement Method for Nuclear and Magnetic Structures. *J. Appl. Crystallogr.* **1969**, *2*, 65–71. [CrossRef]
46. Aoki, K.; Memezawa, A.; Masumoto, T. Amorphization of Ti-Zr Powders by Mechanical Alloying in H₂, N₂ and O₂ Atmospheres. *Mater. Sci. Eng.* **1994**, *181*, 1263–1267. [CrossRef]
47. Ustinovshikov, Y.; Pushkarev, B.; Sapagina, I. Phase Transformations in Alloys of the Fe–V System. *J. Alloys Compd.* **2005**, *398*, 133–138. [CrossRef]
48. Hayakawa, M.; Kuntani, N.; Oka, M. Structural Study on the Tetragonal to Monoclinic Transformation in Arc-Melted ZrO₂-2mol.%Y₂O₃—I. Experimental Observations. *Acta Metall.* **1989**, *37*, 2223–2228. [CrossRef]
49. Leib, E.W.; Pasquarelli, R.M.; Blankenburg, M.; Müller, M.; Schreyer, A.; Janssen, R.; Weller, H.; Vossmeier, T. High-Temperature Stable Zirconia Particles Doped with Yttrium, Lanthanum, and Gadolinium. *Part. Part. Syst. Charact.* **2016**, *33*, 645–655. [CrossRef]
50. Sathiyamoorthi, P.; Basu, J.; Kashyap, S.; Pradeep, K.G.; Kottada, R.S. Thermal Stability and Grain Boundary Strengthening in Ultrafine-Grained CoCrFeNi High Entropy Alloy Composite. *Mater. Des.* **2017**, *134*, 426–433. [CrossRef]
51. Sheikh, S.; M'Saoubi, R.; Flasar, P.; Schwind, M.; Persson, T.; Yang, J.; Llanes, L. Fracture Toughness of Cemented Carbides: Testing Method and Microstructural Effects. *Int. J. Refract. Met. Hard Mater.* **2015**, *49*, 153–160. [CrossRef]
52. Li, W.; Liaw, P.K.; Gao, Y. Fracture Resistance of High Entropy Alloys: A Review. *Intermetallics* **2018**, *99*, 69–83. [CrossRef]
53. Menapace, C.; Cipolloni, G.; Hebda, M.; Ischia, G. Spark Plasma Sintering Behaviour of Copper Powders Having Different Particle Sizes and Oxygen Contents. *Powder Technol.* **2016**, *291*, 170–177. [CrossRef]
54. Sundgren, J.-E. Formation and characterization of titanium nitride and titanium carbide films prepared by reactive sputtering. In *Linköping Stud. Sci. Technol. Diss. No. 79*; Dep. Phys. Meas. Technol. Linköping Inst. Technol.: Linköping, Sweden, 1982; Available online: https://inis.iaea.org/collection/NCLCollectionStore/_Public/13/693/13693374.pdf (accessed on 23 June 2023).
55. Mary, C.; Le Mogne, T.; Beaugiraud, B.; Vacher, B.; Martin, J.M.; Fouvry, S. Tribochemistry of a Ti Alloy under Fretting in Air: Evidence of Titanium Nitride Formation. *Tribol. Lett.* **2009**, *34*, 211–222. [CrossRef]
56. Ettmayer, P.; Kolaska, H. Ti (C, N) Cermets—Metallurgy and Properties. *Int. J.* **1995**, *13*, 343–351. [CrossRef]
57. Taguchi, M.; Sumitomo, H.; Ishibashi, R.; Aono, Y. Effect of Zirconium Oxide Addition on Mechanical Properties in Ultrafine Grained Ferritic Stainless Steels. *Mater. Trans.* **2008**, *49*, 1303–1310. [CrossRef]
58. Gauna, M.R.; Conconi, M.S.; Gomez, S.; Suárez, G.; Aglietti, E.F.; Rendtorff, N.M. Monoclinic-Tetragonal Zirconia Quantification of Commercial Nanopowder Mixtures by XRD and DTA. *Ceram. Silikaty* **2015**, *50*, 318–325.
59. Zhang, Y.; Chen, H.X.; Duan, L.; Fan, J.B.; Ni, L.; Ji, V. A Comparison Study of the Structural and Mechanical Properties of Cubic, Tetragonal, Monoclinic, and Three Orthorhombic Phases of ZrO₂. *J. Alloys Compd.* **2018**, *749*, 283–292. [CrossRef]

Disclaimer/Publisher's Note: The statements, opinions and data contained in all publications are solely those of the individual author(s) and contributor(s) and not of MDPI and/or the editor(s). MDPI and/or the editor(s) disclaim responsibility for any injury to people or property resulting from any ideas, methods, instructions or products referred to in the content.